

Article

Antibacterial TaC-(Fe,Cr,Mo,Ni)-(Ag/Cu) Composite Coatings with High Wear and Corrosion Resistance in Artificial Seawater

Mariya N. Antonyuk ^{*}, Konstantin A. Kuptsov , Alexander N. Sheveyko and Dmitry V. Shtansky 

SEC SHS, National University of Science and Technology "MISIS", Leninsky Prospect 4, 119049 Moscow, Russia

^{*} Correspondence: mariya.antonyuck@ya.ru

Abstract: The synergistic effect of simultaneous mechanical wear, chemical/electrochemical corrosion (tribocorrosion) and microbial attack poses a serious threat to marine and coastal infrastructure. To address this important problem, we have developed composite coatings consisting of TaC (25–35 at.%) and a corrosion-resistant α -Fe(Cr,Ni,Mo)-based metal matrix, as well as bactericidal elements (Cu, Ag). Coatings 50–75 μm thick were obtained by electrospark deposition in vacuum. The coatings possess high hardness (up to 10 GPa) and resistance to cyclic dynamic loads compared with the stainless steel (SS) substrate. Tribocorrosion experiments showed that the decrease in the corrosion potential associated with the removal of a passivating film from the surface during friction was 2–2.5 times smaller for the Ag-containing coating than for the other tested materials. The material passivation rates were also different: almost instantaneous passivation of the Ag- and Cu-doped coatings, and slow passivation for several minutes of the Ag/Cu-free coating and SS. The Ag-containing coating shows the lowest friction coefficient (0.2–0.25) and a minimal wear rate ($1.6 \times 10^{-6} \text{ mm}^3/\text{Nm}$) in artificial seawater. The Ag-doped coating also exhibits the most positive value of corrosion potential and the lowest current density. After exposure in seawater for 20 days, only the Ag-doped coating showed no signs of pitting corrosion. All the studied materials have a pronounced bactericidal effect against *Bacillus cereus* Arc30 bacteria. The resulting coatings can be used to protect steel products from tribocorrosion and fouling in seawater.



Citation: Antonyuk, M.N.; Kuptsov, K.A.; Sheveyko, A.N.; Shtansky, D.V. Antibacterial TaC-(Fe,Cr,Mo,Ni)-(Ag/Cu) Composite Coatings with High Wear and Corrosion Resistance in Artificial Seawater. *Lubricants* **2022**, *10*, 320. <https://doi.org/10.3390/lubricants10110320>

Received: 19 October 2022

Accepted: 18 November 2022

Published: 20 November 2022

Publisher's Note: MDPI stays neutral with regard to jurisdictional claims in published maps and institutional affiliations.



Copyright: © 2022 by the authors. Licensee MDPI, Basel, Switzerland. This article is an open access article distributed under the terms and conditions of the Creative Commons Attribution (CC BY) license (<https://creativecommons.org/licenses/by/4.0/>).

Keywords: electrospark deposition; composite coatings; wear resistance; corrosion resistance; artificial seawater; antibacterial activity

1. Introduction

The development of the ocean and marine space is becoming an increasingly urgent task every year due to the presence of rich natural resources. Parts and equipment of marine and coastal infrastructure, partially or completely submerged in sea water, are exposed to an aggressive environment, which leads to their premature failure [1,2]. The synergistic effect of simultaneous mechanical wear and electrochemical or chemical corrosion (tribocorrosion) in most cases leads to even more serious damage due to the removal of the passivation film and increased corrosive attack [3,4]. Metallic materials are also subjected to the negative effects of the microbiological environment. When they are at rest, bacteria and microorganisms actively develop on their surfaces, which leads to further microbiological corrosion (MBC) [5,6].

Shipbuilding equipment such as propellers, hydraulic turbine blades, shafts, ship winches and parts of water and centrifugal pumps are made of high-strength hardened steels, such as AISI 420S [7]. This material is characterized by high mechanical properties and moderate corrosion resistance [8]. However, the critical components of such equipment are subjected to intensive wear [9], which leads to the removal of the protective oxide film on the surface and an increase in the corrosion rate [10,11]. To minimize wear under tribocorrosion conditions, the material must possess high wear and corrosion resistance.

One of the effective ways to increase wear and corrosion resistance, as well as impart antibacterial activity to materials, is the deposition of coatings [12–16].

Chromium (Cr) is introduced into coatings to increase corrosion resistance and minimize pitting corrosion due to the formation of stable Cr_2O_3 oxide on the surface [17]. Molybdenum (Mo) stabilizes and accelerates passive film formation and increases pitting resistance [18,19]. In a solution containing chlorine ions (Cl^-), Mo reduces the adsorption of these ions on the passive film due to the formation of Mo^{6+} oxide, which reduces the penetration of Cl^- ions. The addition of Ag or Cu to the coating is one of the effective ways to impart antibacterial properties to the surface and, as a result, protect metal parts from biofouling [20]. In addition, the introduction of Ag and Cu makes it possible to improve the tribological properties of coatings due to the formation of a tribolayer based on a solid lubricant during friction [21,22].

Carbides [23,24], nitrides [25,26] and transition metal carbonitrides [27], as well as oxide phases [28,29] such as TaC, TiC, TiN, SiC, TiCN, TiO_2 , Al_2O_3 , ZrO_2 , CeO_2 , WO_3 and Si_3N_4 are often used as hard and wear-resistant structural components in protective coatings. Depending on the required composition, thickness, surface roughness and geometric shape of the items, methods such as electrospark deposition (ESD) in vacuum [12,30], CVD [31,32], PVD [33,34], laser cladding [35,36], galvanic deposition [37,38] and many others are used to deposit protective coatings. Among the listed methods, one should single out the method of electrospark deposition (ESD), which is often used to deposit thick wear-resistant and corrosion-resistant coatings [39]. Vacuum treatment not only allows one to minimize surface oxidation and obtain coatings with high adhesive strength, but also simultaneously implement electrode arc evaporation, which is not realized at atmospheric pressure [40].

For the protection of steels from tribocorrosion, a promising approach is the development of composite coatings consisting of a corrosion-resistant metal matrix based on Fe, Cr, Ni and Mo, additionally alloyed with Cu or Ag to impart antibacterial properties, and reinforcing TaC inclusions. Tantalum carbide TaC was chosen because it has an electrochemical potential ($E_{\text{corr}} = -58$ mV) close to the values of a corrosion-resistant iron-based matrix, preventing the creation of additional galvanic pairs [41]. The aim of this work was to obtain TaC-FeCrMoNi-(Cu/Ag) composite coatings by electrospark alloying in vacuum and to study their corrosion, tribocorrosion, and antibacterial properties in artificial seawater.

2. Materials and Methods

2.1. Electrodes

Electrodes for coating deposition were obtained by cold pressing on a Lab Econ 600 hydraulic press (Fontijne Grotnes BV, Vlaardingen, The Netherlands). For the manufacture of TaC-CrMoNi, TaC-CrMoNi-Cu and TaC-CrMoNi-Ag electrodes, the following powders were used: Cr (PKh-1S, <63 μm), Ni (PNK-0T2, <20 μm), Mo (PM99.95, <5 μm), TaC (MRTU 9-09-03443-77, <5 μm), Cu (PMS-1, <71 μm) and Ag (PS-3, <15 μm , purity 99.0%). The powders were mixed in an Activator-4M planetary mill (Zavod Khimicheskogo Mashinostroeniya, Russia) with a drum volume of 1 L at a powder/balls mass ratio of 1:6 for 4 h. As a result, powder mixtures of three compositions were obtained (at.%): 67.5TaC-12.5Mo-7.5Ni-12.5Cr, 65TaC-10Mo-5Ni-10Cr-10Ag and 65TaC-10Mo-5Ni-10Cr-10Cu. From the resulting mixtures, electrode blanks $7 \times 7 \times 50$ mm^3 in size were obtained at a pressing pressure of 250 MPa. The materials were then sintered in a VE-3-16 vacuum furnace (LLC NPP VakETO, Moscow, Russia) at a pressure of 1×10^{-3} Pa and a temperature of 1300 °C for 60 min. After sintering, the electrodes were ground to obtain rods with a diameter of 6 mm. The composition of the electrodes was as follows (at.%): 37Ta-38C-11Cr-9Mo-5Ni, 36Ta-37C-9Cr-4Mo-4Ni-10Ag and 36Ta-37C-9Cr-8Mo-4Ni-6Cu.

2.2. Deposition of Coatings

Coatings were deposited using an original vacuum installation for electrospark processing [12]. In a vacuum deposition chamber, a 3-axis CNC machine was installed,

equipped with a rotating electrode unit and an insulated brush assembly for supplying voltage. The deposition regimes of the TaC-CrMoNi, TaC-CrMoNi-Cu and TaC-CrMoNi-Ag coatings were chosen after preliminary optimization. It was found that in order to obtain defect-free coatings (without cracks and pores) with high continuity and wear and corrosion resistance, the optimal deposition regimes are as follows: electrode rotation speed 1000 rpm, electrode scanning rate 500 mm/min, scanning step 0.5 mm, electrical pulse frequency 100 Hz, pulse voltage 100 V and pulse duration 50 μ s. Before deposition, the vacuum chamber was evacuated to a pressure of 5×10^{-3} Pa, after which Ar (99.993%) was supplied to the chamber and the operating pressure was maintained at 0.5 Pa. The composition of the as-deposited coatings was as follows (at.%): 34TaC-50Fe-11Cr-3Mo-2Ni, 31TaC-48Fe-10Cr-2Mo-2Ni-7Ag and 24TaC-51Fe-13Cr-3Mo-3Ni-6Cu.

Discs made of 420S steel ($\varnothing 30 \times 4$ mm) were used as substrates. The 420S steel was chosen because it is martensitic steel capable of hardening and possesses moderate corrosion resistance, and in this work we mainly focus on highly loaded elements that require additional protection against corrosion and wear.

2.3. Coatings Characterization

The structural, elemental and phase composition of the electrodes and coatings were studied by scanning electron microscopy (SEM) using an S-3400N microscope (Hitachi) equipped with a NORAN energy-dispersive detector and X-ray diffraction (XRD) using a D8 Advance diffractometer (Bruker).

Hardness (H) and Young's modulus (E) were evaluated by nanoindentation using a Nano Hardness Tester (CSM Instruments) on the coating cross-sections. Before measurements, the tip of the Berkovich diamond indenter was calibrated against fused quartz. The maximum indentation load was set at 8 mN. The measurement error did not exceed 10%. Resistance to cyclic, impact-dynamic loads was studied on an impact tester (CemeCon). The tests were carried out for 10^5 cycles at a frequency of 50 Hz (constant parameter of the device) and a load of 500 N. These regimes are optimal for evaluating the fatigue strength of "hard coating/hard substrate" systems and were successfully used in our previous works [42]. A cemented carbide WC-6Co ball, 5 mm in diameter, was used as a counterbody due to its high strength and fracture toughness, which results in minimal wear of the counterbody during testing. Each sample was tested both in air and in artificial seawater (ASW).

Tribocorrosion properties were studied in ASW using a pin-on-disc tribometer (CSM Instruments) equipped with a rotating three-electrode cell, which allows electrochemical measurements to be carried out both under stationary conditions and during tribological tests. The cell was equipped with an Ag/AgCl reference electrode and an auxiliary Pt electrode. Potentiodynamic measurements were carried out using a VoltaLab PST050 potentiostat (Radiometer Analytical) with coating surface polarization from -200 to $+1000$ mV relative to the open corrosion potential (OCP) at a scanning rate of 1 mV/s. All potentials were recalculated and presented relative to the standard hydrogen electrode. The corrosion current density (CCD) was calculated using the Tafel equation. Artificial seawater was prepared according to ASTM D 1141-98 (Table 1). Instead of cemented carbide, an alumina ball (Al_2O_3) with a diameter of 6 mm and a roughness of 0.8 μ m was used as a counterbody in all ASW experiments because it is a non-conductive and corrosion resistant material and does not affect the corrosion potential measurements.

Table 1. Elemental composition of "artificial sea water" in accordance with ASTM D1141-98.

	NaCl	MgCl ₂	Na ₂ SO ₄	CaCl ₂	KCl	NaHCO ₃	KBr	H ₃ BO ₃	SrCl ₂	NaF
Concentration, g/L	24.53	5.20	4.09	1.16	0.695	0.201	0.10	0.027	0.003	0.003

The tests were carried out at a load of 5 N, a sliding speed of 10 cm/s, and a test distance of 1000 m. The recovery rate of corrosion potential was observed during short pauses (up to 10 min) without rotation.

Coating wear rates were calculated by analyzing the wear track profiles using a Wyko-NT110 optical profiler (Veeco, Plainview, NY, USA). Due to the high roughness of the coatings, the relief of the coatings was smoothed to a roughness (Ra) of less than 1 μm before tribocorrosion tests in order to determine and compare the wear rates of the coatings.

The antibacterial activity of the coating was assessed by counting the number of colony-forming units (CFUs) of gram-positive *Bacillus cereus* Arc30 strain (collection of the State Scientific Center for Applied Microbiology and Biotechnology). Bacterial strains were cultivated on Mueller Hinton solid nutrient agar (HiMedia, India). Prior to the experiments, all plates were sterilized by UV radiation (exposure 60 min, distance 15 cm). One sample of each type was placed in 4 mL of saline, and two wells without samples with 4 mL of saline were used as controls (K). Simultaneously, 0.05 mL of a suspension of a 3-h broth culture of the test strain in saline with a cell concentration of about 2×10^6 CFUs/mL was added to all wells. The samples were incubated in a thermostat at 37 °C. All manipulations were carried out under aseptic conditions, the slightest contact between the samples being avoided. After 0 h, 3 h, 8 h and 24 h, 0.04 mL was taken from each well to determine the concentration of CFUs. Determination of the concentration of CFUs/mL was carried out according to the method of decimal dilutions in 0.3 mL of saline. A 0.01 mL bacterial suspension was inoculated from each dilution into Petri dishes with Mueller Hinton Agar nutrient medium (HiMedia, India), dried in a closed dish at room temperature for 10 min and cultured at 37 °C for 24 h.

3. Results and Discussion

3.1. Structure and Composition of Electrodes and Coatings

When the substrate surface is treated with an electrode, part of the melt, which is a mixture of the substrate and electrode materials, crystallizes at the end of the electrode, forming a secondary structure. Further coating deposition is mainly carried out by mass transfer of this secondary structure. Figure 1 shows SEM images of cross-sections of TaC-CrMoNi-(Cu/Ag) electrodes after ESD in vacuum with corresponding energy dispersive X-ray spectroscopy (EDXS) elemental maps. Two characteristic zones can be distinguished in all electrodes, corresponding to the initial structure after sintering (zone A) and the secondary structure (zone B). The structure of zone A is characterized by TaC grains 1–5 μm in size located in a metal matrix. In addition, Cr and Mo agglomerates are observed in zone A. In zone B, the size of carbide grains is much smaller (0.25–1.5 μm). Compared with the original structure, the distribution of all elements in zone B is more uniform, due to multiple melting, mixing the electrode and substrate materials and subsequent secondary carbide precipitation from the melt. The iron content in the secondary structure is in the range of 28–38 at.% (Table 2).

Table 2. Elemental composition of TaC-CrMoNi-(Cu/Ag) electrodes (at.%).

Electrode	Structure	Ta	C	Mo	Ni	Fe	Cr	Ag	Cu
TaC-CrMoNi	Initial	37	38	9	5	-	11	-	-
	Secondary	21	22	4	4	38	11	-	-
TaC-CrMoNi-Ag	Initial	36	37	4	4	-	9	10	-
	Secondary	23	24	4	3	30	8	8	-
TaC-CrMoNi-Cu	Initial	36	37	8	4	-	9	-	6
	Secondary	21	23	5	4	28	7	-	12

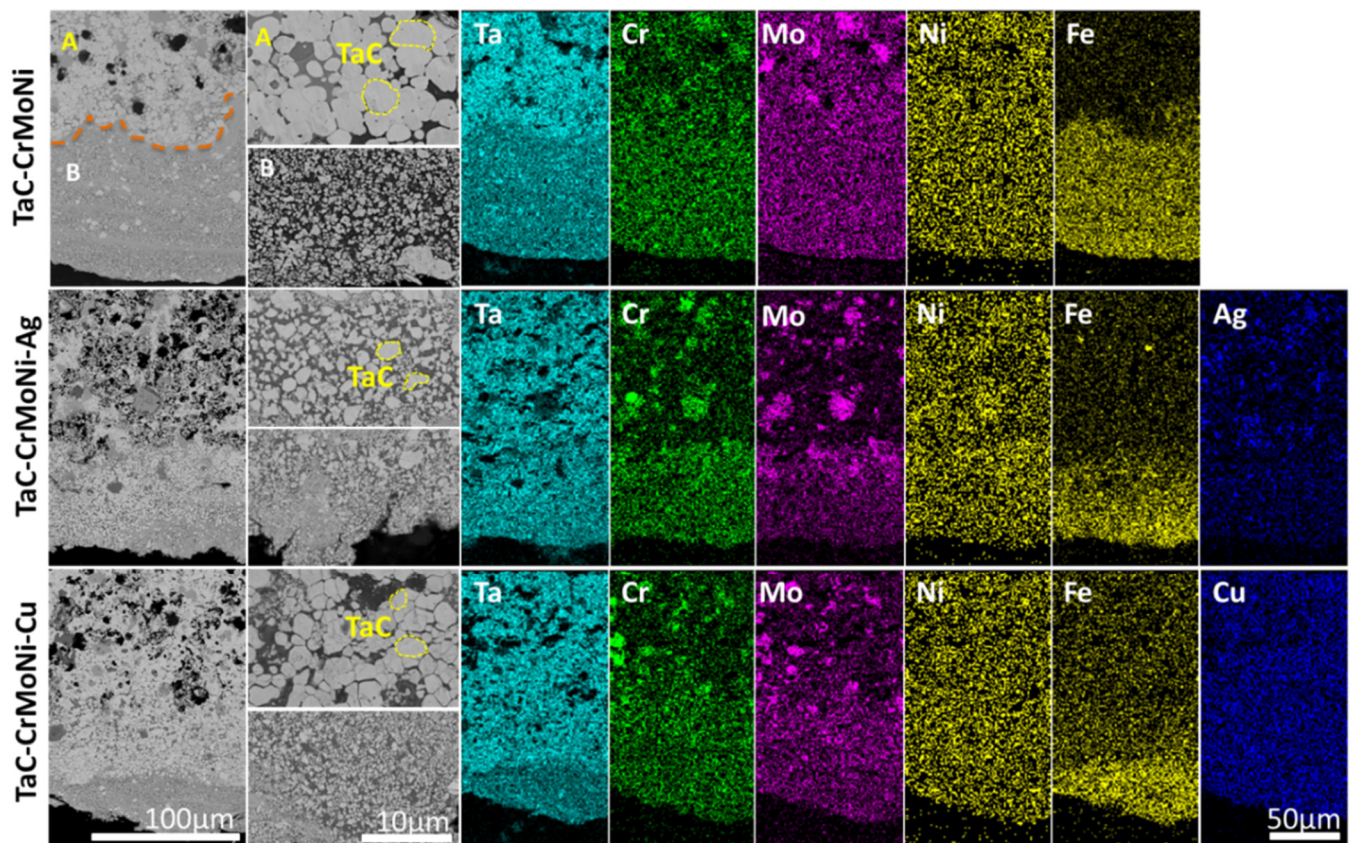


Figure 1. SEM images of initial and secondary structures in TaC-CrMoNi-(Cu/Ag) electrodes with corresponding EDXS elemental maps. Elemental compositions in the marked areas are shown in Table 1.

Figure 2 shows SEM images of the surface (upper row) and cross-section (lower row) of TaC-FeCrMoNi, TaC-FeCrMoNi-Ag and TaC-FeCrMoNi-Cu coatings designated as 1, 2Ag and 3Cu, respectively. The coatings have a dense microstructure without visible defects (Figure 2a,b). Coating 1, with a thickness of approximately 54 μm , consists of carbide grains up to 0.2 μm in size evenly distributed in a metal matrix based on iron. In some areas, larger TaC grains up to 5 μm are observed, surrounded by smaller carbide grains (Figure 2c,d). Coatings 2Ag and 3Cu have a larger thickness of about 75 μm and larger carbide grains with a size of 0.5–3 μm . In the upper part of coating 2Ag, TaC grains have a dendritic morphology. The roughness of each of the as-deposited coatings (R_a) was 9.9 μm , 10.7 μm and 11.8 μm for coatings 3Cu, 1 and 2Ag, respectively.

Table 3 compares the elemental compositions of coatings 1, 2Ag and 3Cu with that of the 420S substrate, determined by the EDXS method. The TaC content in coatings 1 and 2Ag is 31–35%, while when processing with the Cu-containing electrode, the content of TaC is reduced. The coatings contain 48–51% of Fe trapped from the substrate. Note that if we compare the compositions of the 420S steel and the metal matrix of coatings (recalculating the matrix composition by 100% without taking into account Ta and C as components), then the latter contains 4 at.% more Cr. The composition of the metal matrix in all coatings is approximately the same (5 at.% of Mo, 3 at.% of Ni and 17 at.% of Cr).

No silver was found when analyzing the cross-section of coating 2Ag (therefore, the corresponding images are not shown). However, Ag particles 1–4 μm in size were observed on the coating surface (Figure 3a). Silver atoms have high mobility and low reactivity, and therefore do not react with coating elements [43]. During ESD, Ag atoms diffuse to the surface, forming particles [44,45]. In coating 3Cu, copper was observed on the surface in the form of a discontinuous metal layer, as well as segregations inside the coating.

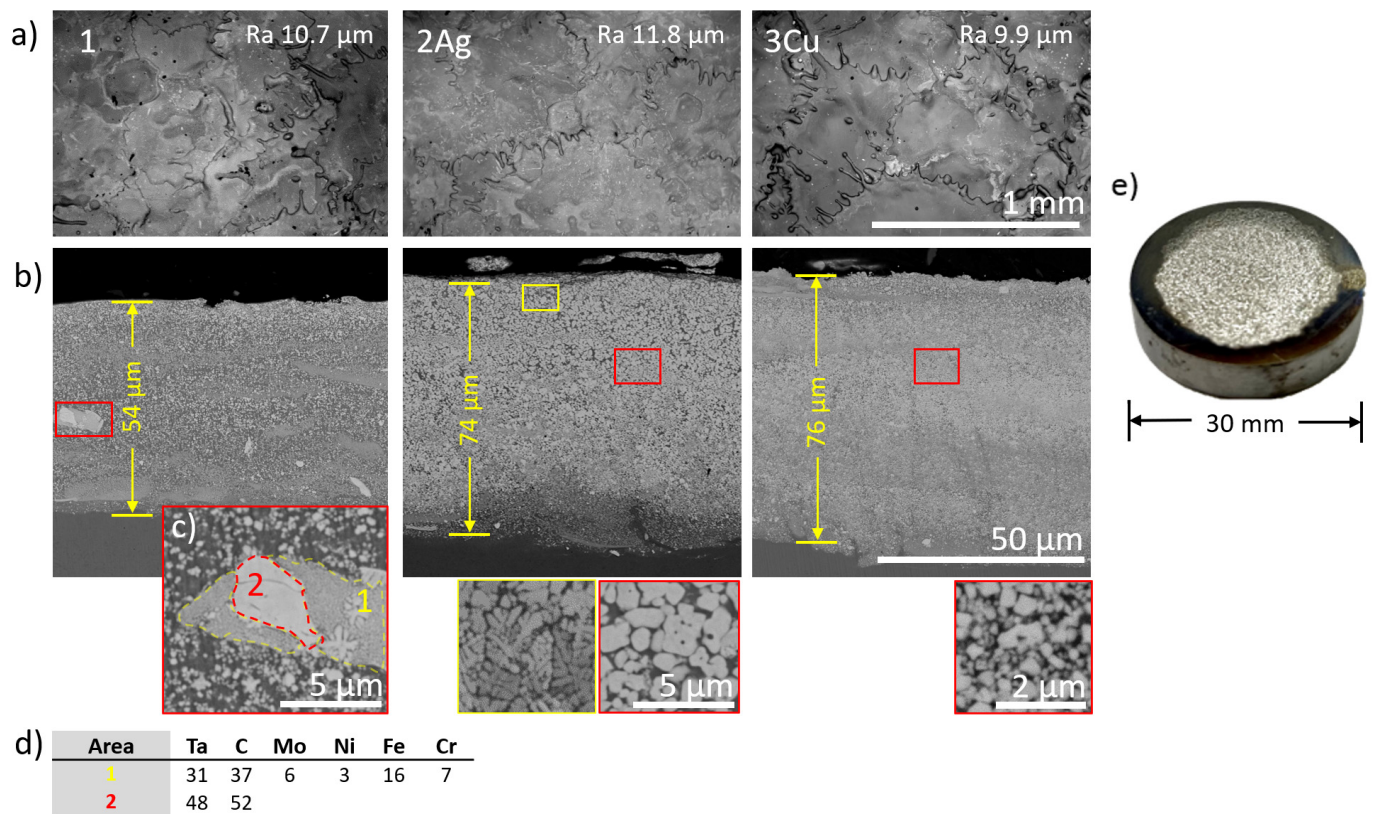


Figure 2. SEM images of the surface (a) and cross-section (b,c) of TaC-FeCrMoNi-(Cu/Ag) coatings. Elemental compositions in areas 1 and 2 (c) are shown in (d) and the typical appearance of the as-deposited samples is shown in (e).

Table 3. Elemental composition of TaC-FeCrMoNi-(Cu/Ag) coatings and 420S substrate (at.%).

	Ta	C	Mo	Ni	Fe	Cr	Cu	Ag
1	16	18	3	2	50	11	-	-
2Ag	15	16	2	2	48	10	-	7
3Cu	11	13	3	3	51	13	6	-
420S	-	-	-	1	86	13	-	-

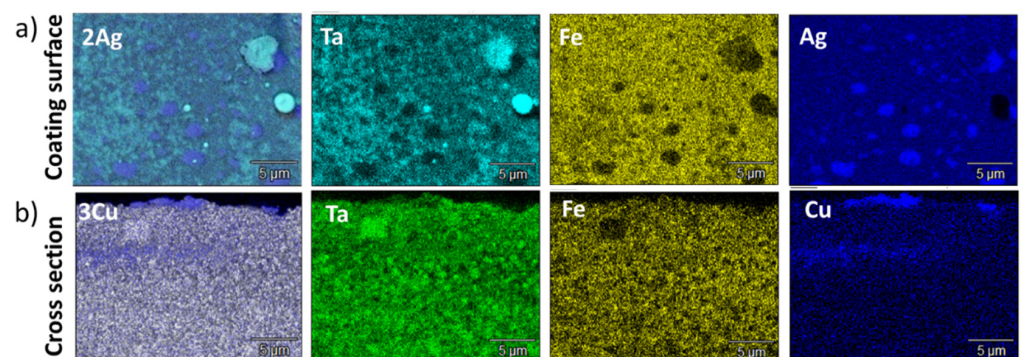


Figure 3. EDXS top-view (a) and cross-sectional (b) elemental maps of coatings 2Ag (a) and 3Cu (b).

Figure 4 presents XRD patterns of coatings 1, 2Ag and 3Cu. All coatings demonstrate two characteristic peaks at 34.9° and 40.5° 2θ , corresponding to the (111) and (200) planes of the fcc TaC phase (ICDD No. 89-3831), as well as a peak at 44.5° due to the presence of an Fe-based solid solution (α -Fe(Cr,Ni,Mo)). An additional peak in coating 2Ag at 38.2° 2θ

occurs as a result of the reflection of X-rays from the (111) planes of the metallic Ag (ICDD no. 87-0720). The peaks at 43.3° and 50.4° 2θ in coating 3Cu correspond to the (111) and (200) planes of metallic Cu (ICDD no. 04-0836).

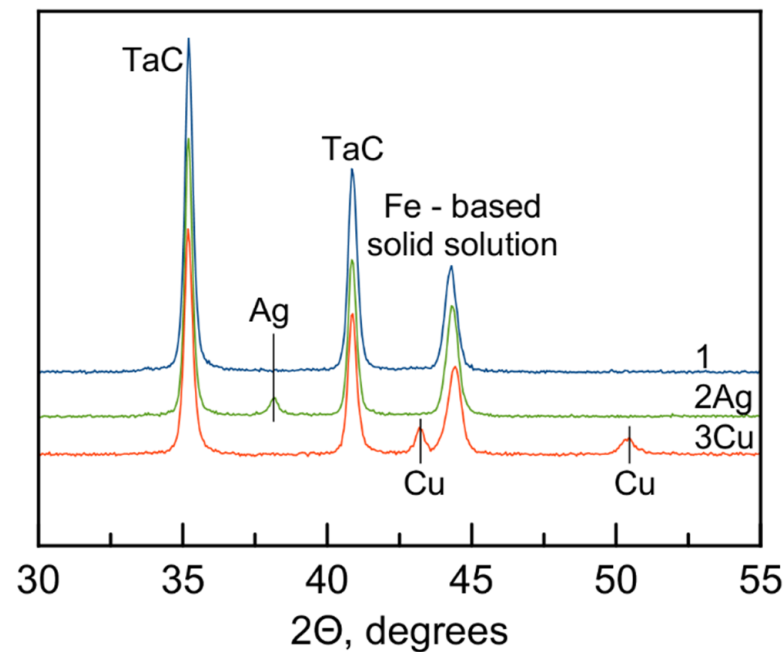


Figure 4. XRD patterns of TaC-FeCrMoNi-(Cu/Ag) coatings.

The hardness (H) and Young's modulus (E) values of the TaC-FeCrMoNi-(Cu/Ag) coatings and the steel substrate are presented in Table 4. The SS substrate has a hardness of 3.7 GPa and a Young's modulus of 210.6 GPa. Coating 1 shows the highest H and E values (10.3 GPa and 278 GPa, respectively). The introduction of Ag and Cu into the coatings led to a decrease in H and E values to 5.9 GPa and 244 GPa (2Ag) and to 8.6 GPa and 250 GPa (3Cu), respectively. The deterioration of mechanical properties can be explained by the presence of soft metals on the coating surfaces [46].

Table 4. Hardness (H) and Young's modulus (E) of TaC-FeCrMoNi-(Cu/Ag) coatings.

	H , GPa	E , GPa
420S	3.7 ± 0.1	210 ± 3.2
1	10.3 ± 0.7	278 ± 4.3
2Ag	5.9 ± 0.6	244 ± 2.2
3Cu	8.6 ± 0.8	250 ± 3.4

3.2. Tribocorrosion Tests

Figure 5 shows friction coefficient (CoF) and OCP versus sliding path during the tribocorrosion testing of coatings 1, 2Ag and 3Cu and a steel substrate in ASW. At rest, coatings 1, 2Ag and 3Cu showed positive OCP values of +50 mV, +40 mV, and +60 mV, respectively, while the substrate potential was more negative (about 0 V). With the onset of friction, a sharp negative increase in the OCP was observed due to the removal of the passivating film [13]. Coating 2Ag showed the smallest potential drop, down to -65 mV, while the OCP of the other coatings decreased more noticeably, to -160 (1) and -130 mV (3Cu). The OCP of the SS substrate during friction was 280 mV.

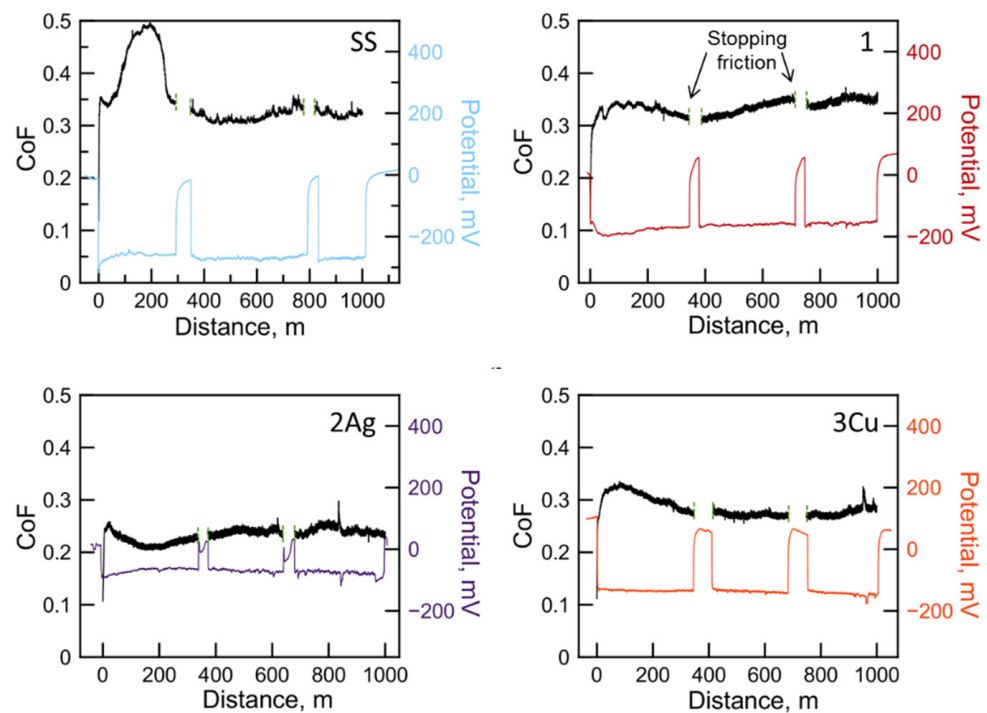


Figure 5. Coefficient of friction and corrosion potential of TaC-FeCrMoNi-(Cu/Ag) coatings and stainless steel substrate versus sliding distance. The tests were carried out in artificial seawater using an Al_2O_3 ball and an applied load of 5 N.

To study the recovery process of the passivating films, the tribological experiments were stopped for approximately 10 min, during which the change in the OCP was recorded. For all studied materials, the OCP increased to the initial values, which indicates the complete recovery of the passivating film. However, the passivation rates of the coatings and the steel substrate were different. Upon the termination of friction, a rapid recovery of corrosion potentials of coatings 2Ag and 3Cu was observed. However, in coating 2Ag, the increase in OCP to values of 0–10 mV was followed by a decrease to approximately -40 mV within a few seconds. It is likely that the initial increase in potential was due to the presence of active Ag particles on the surface, which had a positive potential of $+200$ mV. Subsequently, a silver chloride film quickly formed, and the further formation of a passivating film on the coating surface occurred mainly without the participation of Ag. Coating 1 and the SS substrate showed a gradual increase in OCP to the initial values within 10 min, which is associated with a lower passivation rate.

During the first 200 m of testing in ASW, the CoF of the SS substrate reached 0.5 ± 0.03 , and after running in it stabilized at 0.32 ± 0.02 . Coating 1 had a CoF of about 0.3–0.34. The introduction of Cu and Ag led to a decrease in CoF to 0.27–0.3 and 0.2–0.25, respectively. Figure 6 shows SEM images of the wear tracks of the coatings and the steel substrate after tribocorrosion tests, their 2D profiles, the corresponding wear rates, and the EDXS maps of Ag distribution in coating 2Ag. The wear tracks are not uniform and contain both areas with a tribolayer and areas of complete coating wear, in which the initial TaC grains embedded in the Fe-based metal matrix are observed (Figure 6b). Coatings 1 and 3Cu have similar wear rates of $6.2 \times 10^{-6} \text{ mm}^3/\text{Nm}$ and $5.5 \times 10^{-6} \text{ mm}^3/\text{Nm}$, respectively. The lowest wear rate of $1.6 \times 10^{-6} \text{ mm}^3/\text{Nm}$ was determined for coating 2Ag. The wear rate of the steel substrate is an order of magnitude higher and is $3.7 \times 10^{-5} \text{ mm}^3/\text{Nm}$. The best tribological properties of coating 2Ag are explained by the presence of surficial Ag (Figure 6e), which acts as a solid lubricant during friction. We can assume that in ASW, soft metal (Ag) in the wear track forms a tribolayer composed of silver and corrosion products formed in sea water, which favorably affects the reduction in the friction coefficient due to the synergistic effect of solid/liquid lubricants [47].

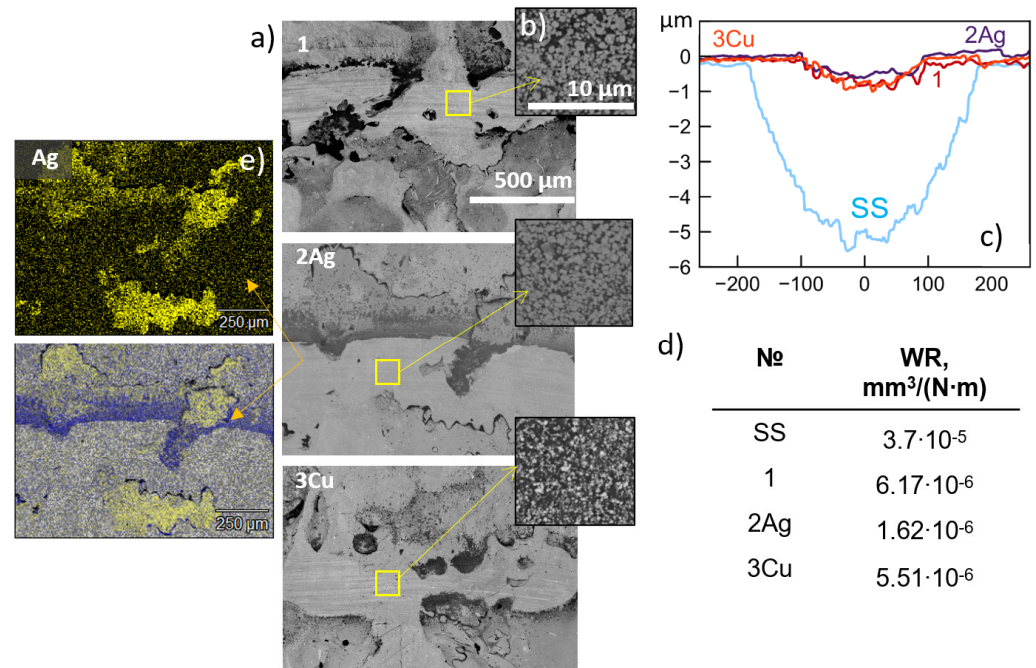


Figure 6. SEM images (a,b) and 2D profiles (c) of wear tracks of coatings 1, 2Ag and 3Cu after tribological tests in artificial seawater with corresponding wear rate values (d) and EDXS Ag maps of coating 2Ag (e).

3.3. Corrosion Tests

To determine the corrosion potential and CCD of the coatings and the steel substrate, further electrochemical studies were carried out with the Tafel extrapolating technique. The obtained results are presented in Figure 7 and Table 5. At the initial stage of electrochemical testing, the coatings are in a passive state. Despite the fact that Tafel calculations have limitations and can give an error [48] when calculating corrosion current density and potential, an almost linear section is observed on the curves in the vicinity of the zero current potential, which indirectly indicates the correctness of the calculations.

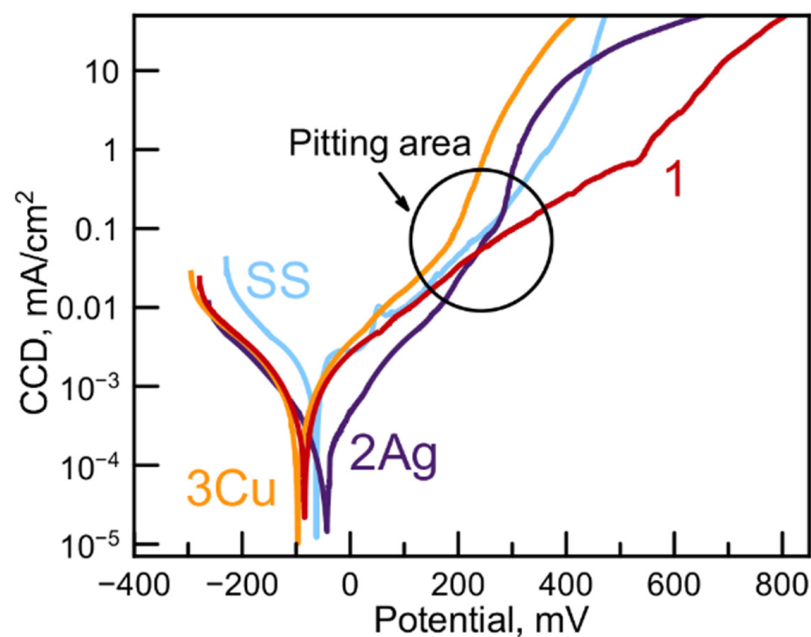


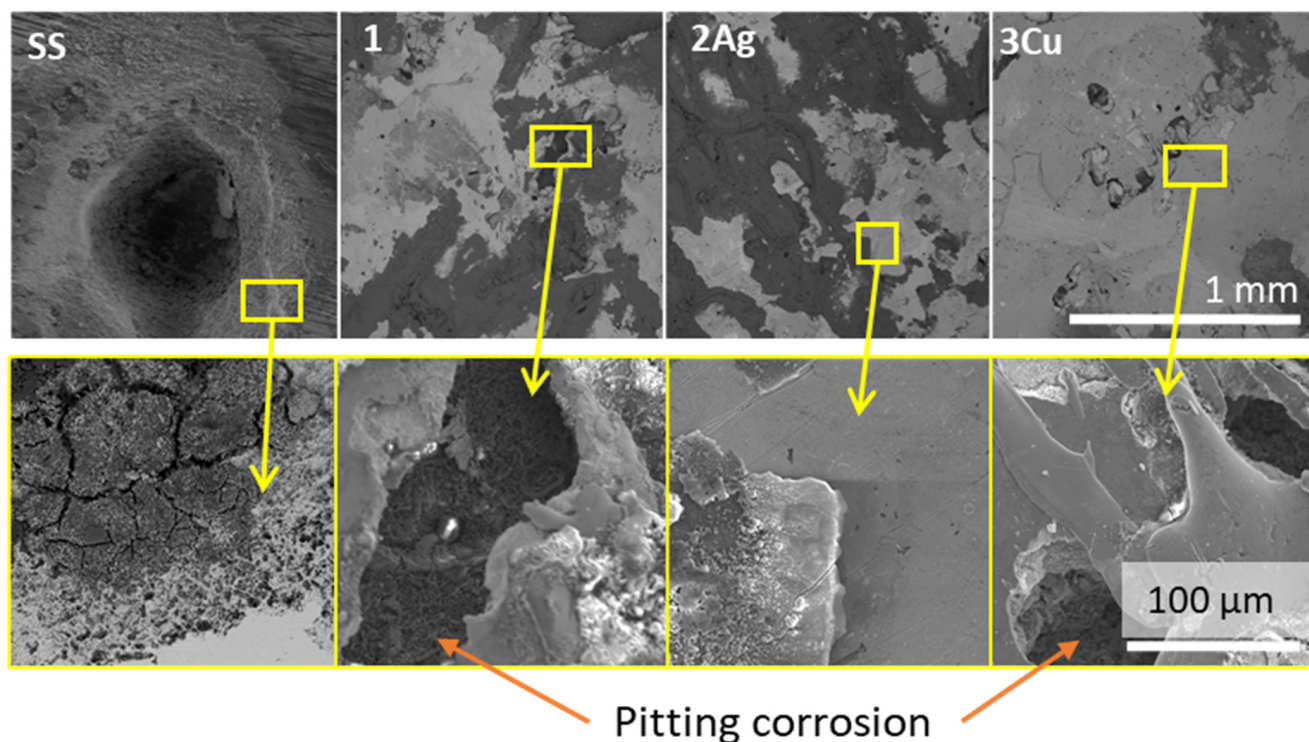
Figure 7. Polarization curves of TaC-FeCrMoNi-(Cu/Ag) coatings and 420S steel substrate.

Table 5. Corrosion potential and corrosion current density of tested coatings and steel substrate.

Sample	OCP, mV	Corrosion Potential (i = 0), mV	Corrosion Current Density, $\mu\text{A}/\text{cm}^2$	Pitting Breakdown Potential, mV
420S	-56 ± 5	-63 ± 5	1.03 ± 0.07	200
1	-82 ± 6	-87 ± 7	0.72 ± 0.06	-
2Ag	-35 ± 4	-43 ± 5	0.17 ± 0.04	260
3Cu	-96 ± 9	-97 ± 8	0.75 ± 0.05	210

The corrosion potentials of the studied materials can be arranged in the following order, starting from the most positive potential: 2Ag coating (-43 mV), steel substrate (-63 mV), coating 1 (-87 mV) and 3Cu coating (-97 mV). In coating 2Ag, a minimum CCD of $0.17 \mu\text{A}/\text{cm}^2$ was observed. The CCDs of coatings 1 and 3Cu were $0.72 \mu\text{A}/\text{cm}^2$ and $0.75 \mu\text{A}/\text{cm}^2$, respectively, both of which are lower than that of steel ($1.0 \mu\text{A}/\text{cm}^2$). With anodic polarization, steel begins to actively dissolve at a potential above $+300$ mV. Coatings 2Ag and 3Cu also showed an increase in CCD upon reaching the dissolution potentials of Ag ($+250$ mV) and Cu ($+150$ mV). Ag- and Cu-free coating 1, at a polarization of more than 200 mV, demonstrated the minimum CCD values. In the potential range of 200 – 230 mV, the curves for coatings 2Ag and 3Cu and the steel substrate showed a bending, which can be attributed to the beginning of pitting breakdown (the values of these potentials are indicated in Table 5). For coating 1, no bending of the potentiodynamic curve was observed.

Figure 8 shows SEM images of the coatings and the steel substrate after exposure to ASW for 20 days. Signs of pitting corrosion were observed both on the surface of coatings 1 and 3Cu and on the steel substrate. However, the characteristic size of the pitting holes on the surface of coatings 1 and 3Cu was significantly smaller ($300 \mu\text{m}$ and $100 \mu\text{m}$, respectively) than those on the steel ($1000 \mu\text{m}$). There were no traces of pitting corrosion on coating 2Ag.

**Figure 8.** SEM surface images of coatings 1, 2Ag and 3Cu and steel substrate after exposure to seawater for 20 days.

3.4. Impact Tests

Figure 9 shows SEM images and 2D profiles of wear craters after impact testing of the coatings and the steel substrate both in air and in ASW at a load of 1000 N for 10^5 cycles. No cracks, delaminations or chips on the edges or inside the craters were observed. The dimensions of the radius and depth of the wear craters are presented in Table 6. The tested materials can be arranged in the following order as the resistance to cyclic impact loads increases: 1 → 3Cu → 2Ag → SS. This is consistent with a decrease in the hardness value of the materials (10.3 GPa → 8.6 GPa → 5.9 GPa → 3.7 GPa). The smallest radii at a depth of wear crater of 9 μm were in coating 1, both when tested in air (280 μm) and ASW (270 μm). Crater sizes and wear track depths were 300 μm and 14 μm (2Ag) and 290 μm and 9 μm (3Cu) when tested in air and 340 μm and 18 μm (2Ag) and 300 μm and 10 μm (3Cu) when tested in ASW. The maximum crater sizes were observed in the SS substrate: 400 μm (radius) and 28 μm (depth) after testing in air and 430 μm and 32 μm after testing in ASW.

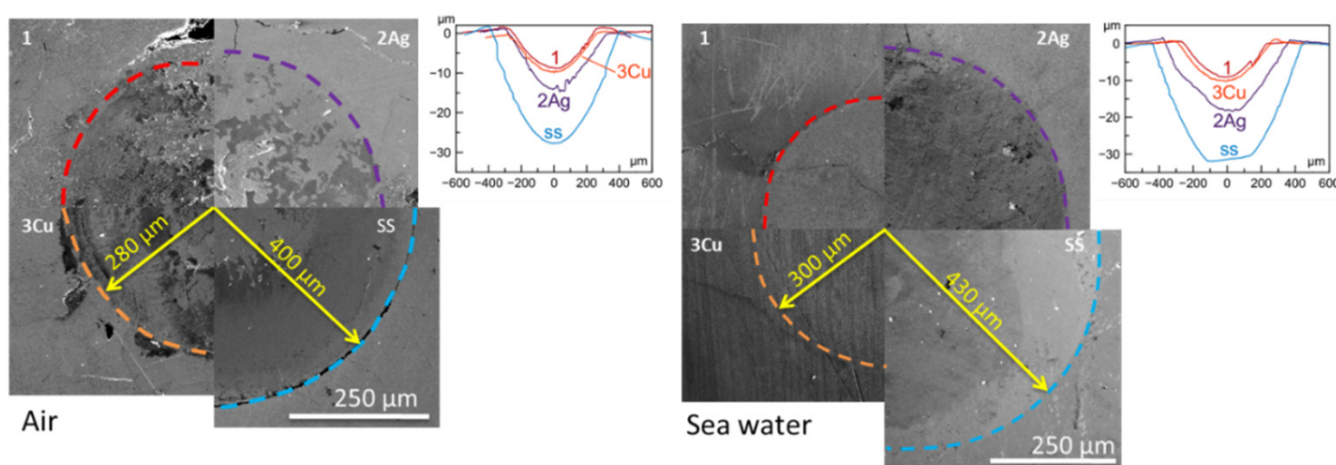


Figure 9. SEM images and 2D profiles of the wear craters of the 2Ag coating and steel substrate after cyclic impact testing in air (left) and artificial seawater (right).

Table 6. Radius (R) and depth (h) of the wear crater of the coatings and steel substrate after cyclic impact-dynamic tests in air and artificial seawater.

Coating	Air		Sea Water	
	R, μm	h, μm	R, μm	h, μm
420S	400	28	430	32
1	280	8.5	270	9
2Ag	300	14	340	18
3Cu	290	9.5	300	10.2

It should be noted that more intense wear of softer materials (SS and coatings 2Ag and 3Cu) was observed during tests in ASW, while the harder coating 1 demonstrated high resistance to cyclic impact-dynamic loads both in air and in ASW. After testing in air, adhering particles of wear products were found in the craters, consisting of metal oxides (oxidized metal particles of the matrix) and tungsten carbide (wear debris of the counterpart material), and after tests in ASW, no wear products were found in the impact craters. It is likely that when testing in ASW, the wear products do not stick to the bottom of the crater, but form a suspension due to hydrodynamic action, which intensifies the abrasive wear [42]. In air, wear debris are stuck to the bottom of the crater, while in water each particle in the suspension moves constantly due to the repeated impact action of the counterbody, which may result in wear of the material at multiple areas of the impact crater.

3.5. Antibacterial Tests

The study of antibacterial activity was carried out using *Bacillus cereus* Arc30 strain. The CFU/mL values at 0 h, 3 h, 8 h and 24 h after inoculation in the presence of coatings 1, 2Ag and 3Cu, as well as the SS substrate and a control without sample (K1), are shown in Figure 10. In the control, K1, the number of surviving CFUs per mL decreased by one order of magnitude from 10^6 to 10^5 after 8 h of incubation, and this level was maintained for 24 h. All the studied coatings and the SS substrate demonstrated a pronounced bactericidal effect. After 3 h and 8 h, an approximately 2-log and 3-log reduction in the CFU/mL, respectively, was achieved. Coatings 1 and 2Ag showed the maximum bactericidal activity after 24 h with almost 4-log reduction in the CFU/mL (99.99% of bacterial cells were inactivated). These results show that adding Ag and Cu does not result in a significant increase in the bactericidal activity against *Bacillus cereus* Arc30 strain.

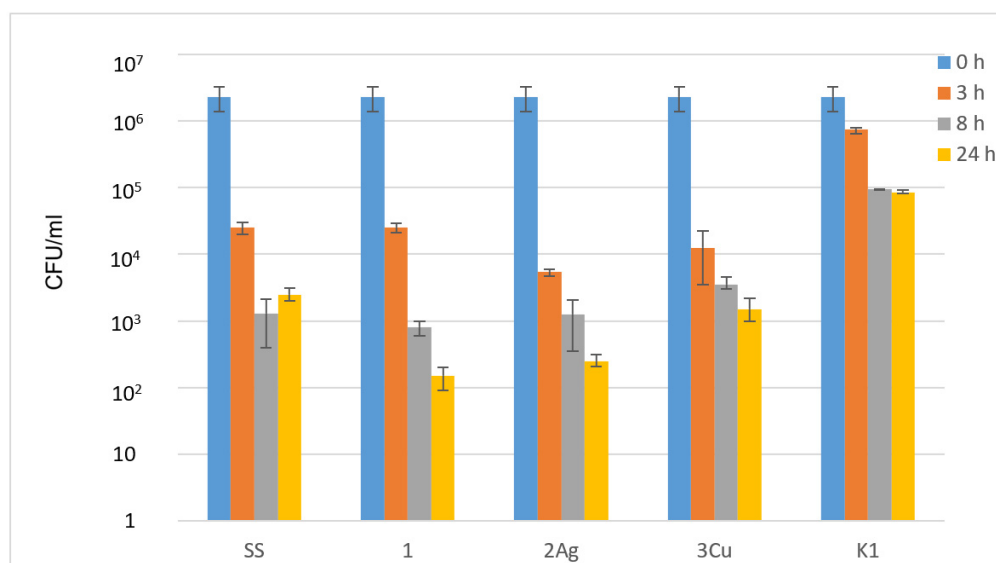


Figure 10. Antibacterial activity of samples against *B. cereus* Arc30 strain, represented as the dependence of CFU/mL on time. SS (stainless steel), TaC-FeCrMoNi coating (1), TaC-FeCrMoNi-Ag coating (2Ag), TaC-FeCrMoNi-Cu coating (3Cu), sample-free well (K1).

4. Discussion

Comparing the data of the electrochemical and tribocorrosion tests, we can draw the following conclusions. The corrosion resistance of coating 1 is mostly determined by the quality of the passive film since TaC carbides are characterized by electrochemical potential close to that of a metal matrix and the effect of galvanic pairs is minimal. In contrast, the Ag and Cu particles on the coatings' surface are active cathodes. In the absence of friction, the Ag- and Cu-containing coatings are more corrosion resistant due to the formation of a higher quality surface passivating film than that of coating 1. However, the distribution of metal particles over the coating surfaces is different. Silver is represented by relatively small particles (up to 2 μm) evenly distributed over the surface. Copper is found both on the surface, in the form of larger particles up to 10 μm , and in the bulk of the coating. In addition, it should be taken into account that Ag particles, unlike Cu, are covered with a thin film of silver chloride. These differences in the composition and distribution of particles determine the coatings' resistance to corrosion.

On the one hand, the presence of Ag and Cu particles leads to the formation of a stable passivating film on the metal matrix. On the other hand, an excess cathode potential at the (Ag, Cu)/matrix interface can lead to the breakdown of the passivating film and the appearance of pitting defects. Large Cu particles form a large potential difference at the interface, which leads to the breakdown of the passivating film and the dissolution of the matrix around the particles. As a result, a relatively high corrosion current and strong

pitting corrosion are observed in coating 3Cu. The Ag-containing coating is characterized by a minimal corrosion current and the absence of pitting corrosion due to the screening of the Ag particles by a chloride film. In this case, there is an optimal combination of the passivation effect of the metal matrix and the low Ag/matrix interface currents that prevents pitting corrosion.

Under tribological contact conditions, the passivating film is constantly removed, the measured potential is determined by the metal matrix potential without the passivating film, and the contribution of passivated regions is small. In this case, the corrosion rate is determined by the recovery rate of the passivating film after its removal by the counterpart material. The maximum drop in potential is observed for SS, since the Cr content, as the main passivating element, is lower compared with the coatings. In the coatings, the recovery rate of the passivating film is determined by the activity of the Ag and Cu particles in the wear track. In coating 1, the potentials between the TaC carbide (-58 mV) and the matrix (-87 mV) are relatively close, so the efficiency of the carbide grains as cathodes is minimal, resulting in the maximum potential drop among the tested coatings. The presence of Cu in the wear track accelerates the surface passivation and results in less potential shift. The minimum potential drop is observed for the Ag-doped coatings and is explained by the fact that Ag has a more positive potential than Cu (i.e., it is a more efficient cathode), and the chloride film that shields Ag under stationary conditions is constantly removed, which accelerates the passivating film recovery. Thus, coating 2Ag demonstrates the maximum resistance under both stationary corrosion and tribocorrosion conditions, since Ag acts as an effective cathode with respect to the metal matrix and promotes more efficient matrix passivation [49].

The coating behavior under cyclic impact-dynamic loads in ASW is different from that under tribological contact conditions. In both cases, the materials are subjected to abrasion, which leads to continuous wear of the passivating film, and corrosive attack, i.e., both types of tests evaluate the resistance of a material to friction, wear, and corrosion. The obtained results show that under impact conditions, the material hardness is the determining factor, and intensive wear of the soft coating components (metallic Ag, Cu and matrix) leads to the leveling of the anticorrosion effects associated with them. In contrast, under tribocontact conditions, an increase in hardness and Young's modulus (in the following order: 2Ag \rightarrow 3Cu \rightarrow 1) leads to a gradual increase both in CoF and wear rate values. In accordance with [50], one may expect that the CoF and wear rate in a "spherical counterbody–plane surface" system would decrease. The observed controversial effect relates to the fact that the decrease in mechanical properties is due to the addition of soft metals (Ag and Cu) to coating 1, which form particles or a discontinuous layer on the surface and act as solid lubricants in sea water. Hence, Ag and Cu not only increase corrosion resistance, but also act as a solid lubricant, resulting in reduced friction and wear.

The potential application of the developed coatings is the protection of steel products operating in aggressive environments containing suspensions of abrasive particles from tribocorrosion, cavitation and biological effects, typical for the infrastructure of the river and sea fleet, hydraulic structures, the equipment of the oil and gas industry and the chemical industry, and manufacturing and sanitary equipment in urban environments.

5. Conclusions

The vacuum electrospark deposition method was successfully applied to produce relatively thick (50–75 μm) tribocorrosion-resistant Ag- and Cu-doped TaC-FeCrMoNi coatings on the surface of AISI 420S steel. The coatings have a composite structure, in which TaC grains 0.2–5.0 μm in size are uniformly distributed in Fe-based metal matrices. Doping with Ag led to the formation of surface particles 1–4 μm in size, while Cu was observed both on the surface and inside the coatings.

The improved corrosion resistance of the coatings was due to the high Cr content and the minimal galvanic effect between the TaC grains and the Fe-based matrix. The Ag-doped coating demonstrated the most positive corrosion potential value and the lowest current

density, and it did not show signs of pitting corrosion after exposure to artificial seawater for 20 days.

The coatings had an increased hardness and wear resistance compared with the substrate and withstood 10^5 cycles in impact-dynamic tests in air and in artificial seawater at a load of 1000 N. The Ag- and Cu-doped coatings showed accelerated passivation in tribocorrosion tests.

The Ag-containing coating had the lowest CoF (0.2–0.25) and the lowest wear rate (1.6×10^{-6} mm³/Nm) in artificial seawater due to the Ag particles acting as a solid lubricant. The Ag- and Cu-doped coatings showed accelerated passivation in tribocorrosion tests.

All coatings exhibited a pronounced bactericidal effect against *Bacillus cereus* Arc30 strain, while the best characteristics were observed for the TaC-(CrMoNi) and TaC-(CrMoNi)-Ag coatings.

Author Contributions: Conceptualization, K.A.K. and A.N.S.; investigation, K.A.K., A.N.S. and M.N.A.; writing—original draft, M.N.A. and K.A.K.; writing—review and editing, D.V.S.; visualization, K.A.K. and M.N.A.; supervision, K.A.K. and D.V.S.; project administration, K.A.K.; funding acquisition, K.A.K. All authors have read and agreed to the published version of the manuscript.

Funding: The work was carried out within the framework of RFBR project No. 20-08-01025, “Investigation of the processes of tribocorrosion, hydroabrasive and cavitation wear of functionally graded coatings for the protection of steels and titanium alloys in seawater”.

Data Availability Statement: Not applicable.

Acknowledgments: The authors are grateful to M.I. Petrzhek for the nanoindentation tests carried out in the Testing Laboratory of Functional Surfaces at NUST «MISIS».

Conflicts of Interest: The authors declare no conflict of interest.

References

1. Sui, X.; Xu, R.; Liu, J.; Zhang, S.; Wu, Y.; Yang, J.; Hao, J. Tailoring the Tribocorrosion and Antifouling Performance of (Cr, Cu)-GLC Coatings for Marine Application. *ACS Appl. Mater. Interfaces* **2018**, *10*, 36531–36539. [[CrossRef](#)] [[PubMed](#)]
2. Melchers, R.E.; Moan, T.; Gao, Z. Corrosion of Working Chains Continuously Immersed in Seawater. *J. Mar. Sci. Technol.* **2007**, *12*, 102–110. [[CrossRef](#)]
3. López-Ortega, A.; Bayón, R.; Arana, J.L. Evaluation of Protective Coatings for Offshore Applications. Corrosion and Tribocorrosion Behavior in Synthetic Seawater. *Surf. Coat. Technol.* **2018**, *349*, 1083–1097. [[CrossRef](#)]
4. Wang, Y.; Zhang, L.; Xiao, J.; Chen, W.; Feng, C.; Gan, X.; Zhou, K. The Tribo-Corrosion Behavior of Cu-9 Wt% Ni-6 Wt% Sn Alloy. *Tribol. Int.* **2016**, *94*, 260–268. [[CrossRef](#)]
5. Chambers, L.D.; Stokes, K.R.; Walsh, F.C.; Wood, R.J.K. Modern Approaches to Marine Antifouling Coatings. *Surf. Coat. Technol.* **2006**, *201*, 3642–3652. [[CrossRef](#)]
6. Zhu, H.; Li, X.; Lu, X.; Wang, J.; Hu, Z.; Ma, X. Efficiency of Gemini Surfactant Containing Semi-Rigid Spacer as Microbial Corrosion Inhibitor for Carbon Steel in Simulated Seawater. *Bioelectrochemistry* **2021**, *140*, 107809. [[CrossRef](#)]
7. Kwok, C.T.; Lo, K.H.; Cheng, F.T.; Man, H.C. Effect of Processing Conditions on the Corrosion Performance of Laser Surface-Melted AISI 440C Martensitic Stainless Steel. *Surf. Coat. Technol.* **2003**, *166*, 221–230. [[CrossRef](#)]
8. Zhang, Z.; Yu, T.; Kovacevic, R. Erosion and Corrosion Resistance of Laser Cladded AISI 420 Stainless Steel Reinforced with VC. *Appl. Surf. Sci.* **2017**, *410*, 225–240. [[CrossRef](#)]
9. Von der Ohe, C.B.; Johnsen, R.; Espallargas, N. Multi-Degradation Behavior of Austenitic and Super Duplex Stainless Steel—The Effect of 4-Point Static and Cyclic Bending Applied to a Simulated Seawater Tribocorrosion System. *Wear* **2012**, *288*, 39–53. [[CrossRef](#)]
10. Pradhan, S.K.; Bhuyan, P.; Bairi, L.R.; Mandal, S. Comprehending the Role of Individual Microstructural Features on Electrochemical Response and Passive Film Behaviour in Type 304 Austenitic Stainless Steel. *Corros. Sci.* **2021**, *180*, 109187. [[CrossRef](#)]
11. Olsson, C.O.A.; Landolt, D. Passive Films on Stainless Steels—Chemistry, Structure and Growth. *Electrochim. Acta* **2003**, *48*, 1093–1104. [[CrossRef](#)]
12. Kuptsov, K.A.; Antonyuk, M.N.; Bondarev, A.V.; Sheveyko, A.N.; Shtansky, D.V. Electrospark Deposition of Wear and Corrosion Resistant Ta(Zr)C-(Fe,Mo,Ni) Coatings to Protect Stainless Steel from Tribocorrosion in Seawater. *Wear* **2021**, *486–487*, 204094. [[CrossRef](#)]
13. Fu, Y.; Zhou, F.; Wang, Q.; Zhang, M.; Zhou, Z. Electrochemical and Tribocorrosion Performances of CrMoSiCN Coating on Ti-6Al-4V Titanium Alloy in Artificial Seawater. *Corros. Sci.* **2020**, *165*, 108385. [[CrossRef](#)]
14. Ma, F.; Li, J.; Zeng, Z.; Gao, Y. Tribocorrosion Behavior in Artificial Seawater and Anti-Microbiologically Influenced Corrosion Properties of TiSiN-Cu Coating on F690 Steel. *J. Mater. Sci. Technol.* **2019**, *35*, 448–459. [[CrossRef](#)]

15. Zhang, M.; Zhou, F.; Wang, Q.; Fu, Y.; Zhou, Z. Tribocorrosion Characteristics of CrMoSiCN/Ag Coatings on Ti6Al4V Alloys in Seawater. *Ceram. Int.* **2021**, *47*, 31780–31797. [[CrossRef](#)]
16. Zhang, M.; Zhou, F.; Fu, Y.; Wang, Q.; Kong, J. Electrochemical Corrosion and Tribological Properties of CrMoCN Coatings Sliding against Al₂O₃ Balls in Artificial Seawater. *Surf. Coat. Technol.* **2021**, *417*, 127225. [[CrossRef](#)]
17. Joy, N.; Sai Venkatesh, B.; Dilip Kumar, S. Microstructure and Corrosion Behavior of Cr-Cu and Cr-Ag Composite Coatings for Industrial Applications. *Mater. Today Proc.* **2021**, *44*, 3697–3700. [[CrossRef](#)]
18. Lee, J.B. Effects of Alloying Elements, Cr, Mo and N on Repassivation Characteristics of Stainless Steels Using the Abrading Electrode Technique. *Mater. Chem. Phys.* **2006**, *99*, 224–234. [[CrossRef](#)]
19. Dalmau, A.; Richard, C.; Igual-Muñoz, A. Degradation Mechanisms in Martensitic Stainless Steels: Wear, Corrosion and Tribocorrosion Appraisal. *Tribol. Int.* **2018**, *121*, 167–179. [[CrossRef](#)]
20. Calabrese, C.; La Parola, V.; Testa, M.L.; Liotta, L.F. Antifouling and Antimicrobial Activity of Ag, Cu and Fe Nanoparticles Supported on Silica and Titania. *Inorganica Chim. Acta* **2022**, *529*, 120636. [[CrossRef](#)]
21. Hsieh, J.H.; Li, C.; Lin, Y.C.; Chiu, C.H.; Hu, C.C.; Chang, Y.H. Antibacteria and Anti-Wear TaN-(Ag,Cu) Nanocomposite Thin Films Deposited on Polyether Ether Ketone. *Thin Solid Films* **2015**, *584*, 277–282. [[CrossRef](#)]
22. Dang, C.; Li, J.; Wang, Y.; Chen, J. Structure, Mechanical and Tribological Properties of Self-Toughening TiSiN/Ag Multilayer Coatings on Ti6Al4V Prepared by Arc Ion Plating. *Appl. Surf. Sci.* **2016**, *386*, 224–233. [[CrossRef](#)]
23. Bin Humam, S.; Gyawali, G.; Amanov, A.; Kim, T.H.; Lee, S.W. Microstructure, Interface, and Nanostructured Surface Modifications to Improve Mechanical and Tribological Performance of Electrodeposited Ni-W-TaC Composite Coating. *Surf. Coat. Technol.* **2021**, *419*, 127293. [[CrossRef](#)]
24. Wang, Q.; Luo, S.; Wang, S.; Wang, H.; Ramachandran, C.S. Wear, Erosion and Corrosion Resistance of HVOF-Sprayed WC and Cr₃C₂ Based Coatings for Electrolytic Hard Chrome Replacement. *Int. J. Refract. Met. Hard Mater.* **2019**, *81*, 242–252. [[CrossRef](#)]
25. Santaella-González, J.B.; Hernández-Torres, J.; Morales-Hernández, J.; Flores-Ramírez, N.; Ferreira-Palma, C.; Rodríguez-Jiménez, R.C.; García-González, L. Effect of the Number of Bilayers in Ti/TiN Coatings on AISI 316L Deposited by Sputtering on Their Hardness, Adhesion, and Wear. *Mater. Lett.* **2022**, *316*, 132037. [[CrossRef](#)]
26. Fang, J.; Piliptsov, D.G.; Bekarevich, R.; Rogachev, A.V.; Jiang, X.; Kulesh, E. Effect of the Alloying Elements in TiN Sublayer on the Structure and Mechanical Properties of Carbon Coatings. *Thin Solid Films* **2022**, *755*, 139324. [[CrossRef](#)]
27. Özkan, D.; Yılmaz, M.A.; Erdem, C.; Türküz, C.; Sulukan, E.; Yağcı, M.B. Wear and Friction Behavior of CrTiN/TiCN and CrTiN/CrCN Multilayer Composite Coatings. *Ceram. Int.* **2022**, *48*, 13732–13747. [[CrossRef](#)]
28. Kim, D.; Jeon, K.; Lee, Y.; Seo, J.; Seo, K.; Han, H.; Khan, S. Preparation and Characterization of UV-Cured Polyurethane Acrylate/ZnO Nanocomposite Films Based on Surface Modified ZnO. *Prog. Org. Coatings* **2012**, *74*, 435–442. [[CrossRef](#)]
29. Choudhury, D.; Rincon, C.; Wei, R.; Benamara, M.; Zou, M. Polydopamine + SiO₂ Nanoparticle Underlayer for Improving DLC Coating Adhesion and Durability. *Surf. Coat. Technol.* **2022**, *429*, 127964. [[CrossRef](#)]
30. Kuptsov, K.A.; Sheveyko, A.N.; Sidorenko, D.A.; Shtansky, D.V. Electro-Spark Deposition in Vacuum Using Graphite Electrode at Different Electrode Polarities: Peculiarities of Microstructure, Electrochemical and Tribological Properties. *Appl. Surf. Sci.* **2021**, *566*, 150722. [[CrossRef](#)]
31. Siddiqui, A.R.; Maurya, R.; Katiyar, P.K.; Balani, K. Superhydrophobic, Self-Cleaning Carbon Nanofiber CVD Coating for Corrosion Protection of AISI 1020 Steel and AZ31 Magnesium Alloys. *Surf. Coat. Technol.* **2020**, *404*, 126421. [[CrossRef](#)]
32. Triana, A.; Olaya, J.J.; Prieto, C. Effect of the Electrolyte Composition on the Corrosion Resistance of Single-Layer CVD-Graphene. *Surfaces and Interfaces* **2022**, *31*, 102025. [[CrossRef](#)]
33. Liao, L.; Gao, R.; Yang, Z.H.; Wu, S.T.; Wan, Q. A Study on the Wear and Corrosion Resistance of High-Entropy Alloy Treated with Laser Shock Peening and PVD Coating. *Surf. Coat. Technol.* **2022**, *437*, 128281. [[CrossRef](#)]
34. Shan, L.; Zhang, Y.R.; Wang, Y.X.; Li, J.L.; Jiang, X.; Chen, J.M. Corrosion and Wear Behaviors of PVD CrN and CrSiN Coatings in Seawater. *Trans. Nonferrous Met. Soc. China* **2016**, *26*, 175–184. [[CrossRef](#)]
35. Aubry, P.; Blanc, C.; Demirci, I.; Gorny, C.; Maskrot, H. Analysis of a Ni-Fe-Cr-Mo-Si Hardfacing Alloy Manufactured by Laser Cladding: Influence of the Iron Content on the Wear Resistance Properties. *Procedia CIRP* **2018**, *74*, 210–213. [[CrossRef](#)]
36. Wen, X.; Cui, X.; Jin, G.; Liu, Y.; Zhang, Y.; Zhang, X.; Liu, E.; Tian, H.; Fang, Y. Corrosion and Tribo-Corrosion Behaviors of Nano-Lamellar Ni_{1.5}CrCoFe_{0.5}Mo_{0.1}Nb_x Eutectic High-Entropy Alloy Coatings: The Role of Dual-Phase Microstructure. *Corros. Sci.* **2022**, *201*, 110305. [[CrossRef](#)]
37. Sriraman, K.R.; Brahimi, S.; Szpunar, J.A.; Osborne, J.H.; Yue, S. Tribocorrosion Behavior of Zn, Zn-Ni, Cd and Cd-Ti Electrodeposited on Low Carbon Steel Substrates. *Surf. Coat. Technol.* **2013**, *224*, 126–137. [[CrossRef](#)]
38. Hamlaoui, Y.; Tifouti, L.; Pedraza, F. On the Corrosion Resistance of Porous Electroplated Zinc Coatings in Different Corrosive Media. *Corros. Sci.* **2010**, *52*, 1883–1888. [[CrossRef](#)]
39. Enrique, P.D.; Marzbanrad, E.; Mahmoodkhani, Y.; Jiao, Z.; Toyserkani, E.; Zhou, N.Y. Surface Modification of Binder-Jet Additive Manufactured Inconel 625 via Electrospark Deposition. *Surf. Coat. Technol.* **2019**, *362*, 141–149. [[CrossRef](#)]
40. Sheveyko, A.N.; Kuptsov, K.A.; Kiryukhantsev-Korneev, P.V.; Kaplansky, Y.Y.; Orekhov, A.S.; Levashov, E.A. Protective Coatings for LPBF Ni-Based Superalloys Using a Combination of Electrospark Deposition and Pulsed Arc Evaporation Methods. *Appl. Surf. Sci.* **2022**, *581*, 152357. [[CrossRef](#)]
41. Zhao, Y.; Xu, J.; Peng, S. Synthesis and Evaluation of TaC Nanocrystalline Coating with Excellent Wear Resistance, Corrosion Resistance, and Biocompatibility. *Ceram. Int.* **2021**, *47*, 20032–20044. [[CrossRef](#)]

42. Kuptsov, K.A.; Kiryukhantsev-Korneev, P.V.; Sheveyko, A.N.; Shtansky, D.V. Comparative Study of Electrochemical and Impact Wear Behavior of TiCN, TiSiCN, TiCrSiCN, and TiAlSiCN Coatings. *Surf. Coat. Technol.* **2013**, *216*, 273–281. [[CrossRef](#)]
43. Hu, J.; Li, H.; Li, J.; Wu, Q.; Huang, J.; Kong, J.; Shi, Y.; Zhang, G.; Xiong, D. Effect of Ag Target Power on Structure, Mechanical Properties of TaC–Ag Films. *Ceram. Int.* **2022**, *48*, 11718–11728. [[CrossRef](#)]
44. Bondarev, A.V.; Kiryukhantsev-Korneev, P.V.; Levashov, E.A.; Shtansky, D.V. Tribological Behavior and Self-Healing Functionality of TiNbCN–Ag Coatings in Wide Temperature Range. *Appl. Surf. Sci.* **2017**, *396*, 110–120. [[CrossRef](#)]
45. Sukhorukova, I.V.; Sheveyko, A.N.; Manakhov, A.; Zhitnyak, I.Y.; Gloushankova, N.A.; Denisenko, E.A.; Filippovich, S.Y.; Ignatov, S.G.; Shtansky, D.V. Synergistic and Long-Lasting Antibacterial Effect of Antibiotic-Loaded TiCaP–CON–Ag Films against Pathogenic Bacteria and Fungi. *Mater. Sci. Eng. C* **2018**, *90*, 289–299. [[CrossRef](#)]
46. Mejía, H.D.; Echavarría, A.M.; Bejarano G., G. Influence of Ag–Cu Nanoparticles on the Microstructural and Bactericidal Properties of TiAlN(Ag,Cu) Coatings for Medical Applications Deposited by Direct Current (DC) Magnetron Sputtering. *Thin Solid Films* **2019**, *687*, 137460. [[CrossRef](#)]
47. Zhu, S.; Yu, Y.; Cheng, J.; Qiao, Z.; Yang, J.; Liu, W. Solid/Liquid Lubrication Behavior of Nickel Aluminum–Silver Alloy under Seawater Condition. *Wear* **2019**, *420–421*, 9–16. [[CrossRef](#)]
48. McCafferty, E. Validation of Corrosion Rates Measured by the Tafel Extrapolation Method. *Corros. Sci.* **2005**, *47*, 3202–3215. [[CrossRef](#)]
49. Zhong, L.; Luo, Y.; Li, Y.; Yang, Y.; Wang, X.; Zhou, T.; Liu, M.; Zhao, Y.; Lai, X.; Bi, J.; et al. Realization of Improved Electrochemical Performance for ZnCo₂O₄/C Nanosheets through Ag Coating. *Ceram. Int.* **2022**, *48*, 16206–16214. [[CrossRef](#)]
50. Bhaumik, S.; Datta, S.; Pathak, S.D. Analyses of Tribological Properties of Castor Oil with Various Carbonaceous Microand Nano-Friction Modifiers. *J. Tribol.* **2017**, *139*, 061802. [[CrossRef](#)]